AD_____

Award Number: DAMD17-01-1-0226

TITLE: New Approaches in SPECT Breast Imaging

PRINCIPAL INVESTIGATOR: Kelly Braun
R. Jaszczak, Ph.D.
K. Bobkov, Ph.D.
J. Bowsher, Ph.D.

CONTRACTING ORGANIZATION: Duke University
Durham, North Carolina 27708-0077

REPORT DATE: July 2004

TYPE OF REPORT: Annual Summary

PREPARED FOR: U.S. Army Medical Research and Materiel Command
Fort Detrick, Maryland 21702-5012

REPORT DOCUMENTATION PAGE

Form Approved
OMB No. 074-0188

1. AGENCY USE ONLY (Leave blank)	2. REPORT DATE	3. REPORT TYPE AND DATES COVERED
	July 2004	Annual Summary (1 Jul 01-30 Jun 04)

4. TITLE AND SUBTITLE
New Approaches in SPECT Breast Imaging

5. FUNDING NUMBERS
DAMD17-01-1-0226

6. AUTHOR(S)
Kelly Braun
R. Jaszczak, Ph.D.
K. Bobkov, Ph.D.
J. Bowsher, Ph.D.

7. PERFORMING ORGANIZATION NAME(S) AND ADDRESS(ES)
Duke University
Durham, North Carolina 27708-0077

E-Mail: keb21@duke.edu

8. PERFORMING ORGANIZATION REPORT NUMBER

9. SPONSORING / MONITORING AGENCY NAME(S) AND ADDRESS(ES)
U.S. Army Medical Research and Materiel Command
Fort Detrick, Maryland 21702-5012

10. SPONSORING / MONITORING AGENCY REPORT NUMBER

11. SUPPLEMENTARY NOTES
Original contains color plates. All DTIC reproductions will be in black and white.

12a. DISTRIBUTION / AVAILABILITY STATEMENT
Approved for Public Release; Distribution Unlimited

12b. DISTRIBUTION CODE

13. ABSTRACT (Maximum 200 Words)

The primary objective of this research is to develop new techniques in single photon emission computed tomography (SPECT) breast cancer imaging providing improved detection and characterization of early stage breast cancer. Projection data were acquired by implementing a tiltable SPECT system on a breast and torso phantom. The data were reconstructed with both an ordered subset expectation maximization (OSEM) algorithm and a filtered backprojection (FBP) algorithm with a ramp filter. Results indicated that the OSEM values for SNR and contrast were higher at all tilt angles and may offer better shape and uniform activity distribution of the breast compared to FBP images. Also, by using a tilted head SPECT system, the radius of rotation decreases and the chest wall near the breast can be adequately imaged. This results in increased resolution and sensitivity. A pinhole collimator is advantageous in imaging a breast due to its ability to get close to the breast and achieve a small radius of rotation, though lead shielding was ineffective in eliminating background activity from the myocardium and liver. Combining a pinhole collimator with a tiltable head camera (T-22 SPECT) will hopefully provide us with improved resolution and increased angular range.

14. SUBJECT TERMS
Nuclear medicine, single photon emission computed tomography (SPECT), OSEM, filtered backprojection, breast imaging, Orlov

15. NUMBER OF PAGES
23

16. PRICE CODE

17. SECURITY CLASSIFICATION OF REPORT	18. SECURITY CLASSIFICATION OF THIS PAGE	19. SECURITY CLASSIFICATION OF ABSTRACT	20. LIMITATION OF ABSTRACT
Unclassified	Unclassified	Unclassified	Unlimited

Table of Contents

Cover.....1

SF 298.....2

Introduction.....4

Body.....4

Key Research Accomplishments.....6

Reportable Outcomes.....6

Conclusions.....7

References.....7

Appendices.....7

INTRODUCTION

The primary objective of this research centered around breast cancer imaging, specifically developing new techniques in single photon emission computed tomography (SPECT) breast cancer imaging which will provide improved detection and characterization of breast cancer. The leading hypothesis in this research is that by using a vertical axis of rotation (VAOR) and various camera head and collimator configurations, several advantages can be gained over traditional horizontal axis of rotation (HAOR) SPECT. A tiltable head SPECT (TH-SPECT) system allows for improved imaging of lesions closer to the chest wall as well as a smaller radius of rotation [1]. Compared to a filtered backprojection reconstruction algorithm, OSEM reconstruction algorithm displayed improved images [3]. The use of a pinhole collimator allows for less background activity to be detected, a smaller radius of rotation, and higher values for contrast and SNR [4].

BODY

Disadvantages of HAOR breast imaging with SPECT include attenuation through the torso and a large radius of rotation (ROR). Tilting a camera head allows the collimator to get closer to the breast and chest wall. Using various tilt angles for the camera heads, an axially Tiltable 2-Headed SPECT (TH-SPECT) system was used to observe resolution, contrast and SNR values in fillable breast and torso phantoms containing a 1 cm lesion suspended in the breast. The results of this HAOR TH-SPECT system were compared to high-count planar images. An ordered subsets expectation maximization (OSEM) algorithm (8 subsets, 3 iterations), which accounted for the geometry of the system, was used to reconstruct the data. In comparison to the high count planar images, a 0.5mL lesion was more clearly visible in TH-SPECT. Lesion contrast and lesion SNR improved nearly three and two times, respectively. As a result, this system configuration reduced the radius of rotation and allowed for adequate imaging near the chest wall breast tissue, improving sensitivity and resolution [1]. A more detailed description of these results can be found in the appendix in "Breast Tumor Imaging Using Tiltable Head SPECT Cameras." The one drawback to this system is the fact that axially blurring affects the chest wall region of the breast. Future work could be done with a combination of two heads tilting at different angles, aiming to provide more complete sampling.

One concern dealing with TH-SPECT that was evident in the previous study dealt with insufficient axial sampling of the image space. Specifically, insufficient sampling of the myocardium, liver and torso will cause interference when imaging small lesions in the breast and thus result in artifacts in the reconstructed images. Tilting the camera head prevents the reconstruction algorithms from meeting the Orlov sphere requirement, which states that an image space must be sampled over a great circle [2]. A three-dimensional algorithm is needed to reconstruct TH-SPECT data. Iterative methods, such as OSEM, have been used to model the sampling of frequency space associated with circular orbits with a tilted geometry. In the following research, a filtered backprojection (FBP) algorithm was devised with the intent of successfully reconstructing tilted-head geometries. This FBP method was compared to OSEM for a fillable breast phantom containing lesions at various tilt angles and for a fillable breast phantom containing a mini-Defrise disk imaged with parallel-beam TH-SPECT at angles of 0-15 degrees. Values for

both contrast and SNR were compared. The publication supporting this research can be found in the appendix. In this paper [3], a geometric derivation of the ramp filter is presented for tilted parallel beam geometries. Using this ramp filter, a FBP method was implemented and compared with an iterative OSEM algorithm using TH-SPECT data. The FBP results indicated a greater increase in backprojection artifacts with greater angular tilt, as well as a greater bias in FBP noise versus bias plots with a greater angular tilt. OSEM reconstructions showed greater SNR and contrast values at all tilt angles [3]. Because TH-SPECT data do not sufficiently sample the Orlov sphere, artifacts are present in all reconstructions. However, OSEM TH-SPECT reconstruction offers better shape and uniform activity distribution of the breast compared to FBP methods [3].

A pinhole collimator is advantageous over a parallel-hole collimator in imaging the breast in its ability to decrease the ROR, resulting in better resolution for detecting lesions. However, an issue in both parallel and pinhole SPECT breast imaging is photon contamination from other organs that will impact the clarity of the image, such as the liver, myocardium, lungs and gall bladder. Since a pinhole collimator, due to its geometry, will collect fewer photons from the torso, the hypothesis that we set out to prove was that lead shielding on the bed would further reduce the unwanted photons from outlying organs that were collected by the pinhole collimator and thus increase the contrast and SNR of the image. Using a Trionix XLT scanner (Trionix Research Lab, Twinsburg, Ohio) with one pinhole collimator, experimental data was obtained of a breast phantom mounted on an anthropomorphic torso phantom placed in a prone position on the bed (Figure 1). The first set of scans consisted of the torso phantom and all its organs filled with activity, and the second set of scans consisted of the same configuration of the torso phantom as the first scan, except with the addition of lead shielding placed over the entire table except for where the breast was located. The angular range of these scans was 186 degrees, resulting in an incomplete circular orbit (ICO). The breast contained two spherical lesions (1.6 cm diameter), both of which were filled with activity. The projection data were reconstructed, without shielding attenuation modeling or scattering and attenuation correction, with an OSEM algorithm having thirty iterations and eight subsets. A 3-D region-of-interest analysis was performed on the lesions to evaluate shielding effects. The use of shielding slightly reduced noise in contrast estimates, from about 0.25 to 0.23. However, shielding increased bias in contrast from 0.24±0.08 to 0.44±0.07. SNRs were also lower with shielding. These results suggest that if shielding is to be of benefit, shielding attenuation must be modeled within iterative reconstruction. However, the standard reconstruction algorithms such as OSEM and MLEM are limited in reconstructing inconsistent projection data. An abstract [4] and supplementary information was submitted accepted to the 2004 NSS/MIC conference and is also attached for a more detailed explanation of this experiment.

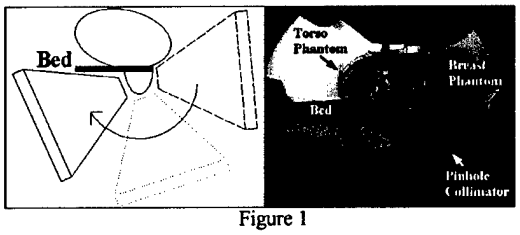

Figure 1

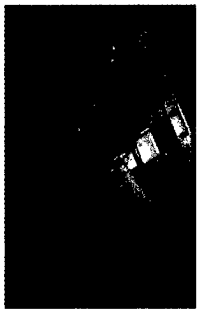
Figure 2

An advantage of the Summit T-22 SPECT system, shown in Figure 2, is the fact that the camera heads can be tilted through varying angles. Currently, the T-22 can only use parallel collimators. To tie together all the previous research, we want to use a tiltable head system with a small radius of rotation in conjunction with a pinhole collimator to image the breast. In order to use

the pinhole collimator in conjunction with the T-22 camera, we have designed an adaptor plate, shown in Figure 3, to allow the pinhole collimator to be mounted onto the camera. This plate was designed using Computer Assisted Design and is in the process of being built by the Duke University Physics Shop. There are actually two plates being built, one for each of the detector heads on the T-22 system. Once these plates are finished, the pinhole collimator can be attached to the T-22 system and used to image the breast. For the acquisition of experimental VAOR phantom studies, two pinhole collimators would be mounted on the two tilted detector heads. A different tilt-angle would be used for each detector head.

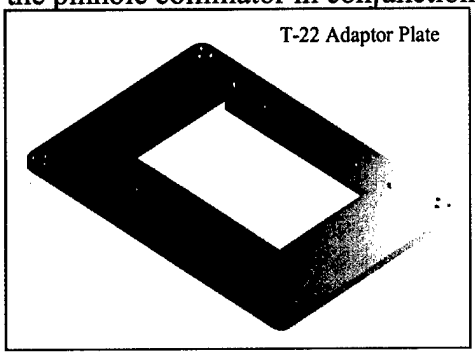

Figure 3

KEY RESEARCH ACCOMPLISHMENTS

- Development and evaluation of FBP TH-SPECT image reconstruction algorithm using a geometric derivation of the ramp filter [3].
- Comparison of FBP TH-SPECT algorithm with traditional FBP and OSEM [3].
- Acquisition, evaluation, and comparison of TH-SPECT data, including contrast and S/N analysis using experimental phantoms [1].
- Acquisition and evaluation of combined horizontal and vertical axes of rotation.
- Comparison of contrast and SNR values between shielded and unshielded torso phantom [4].
- Design of special adapter plate for using Triad XLT pinhole collimator on T22 SPECT system.

REPORTABLE OUTCOMES:

Manuscripts

- Pieper BC, Bowsher JE, Tornai MP, Archer CN, Jaszczak JJ, Parallel-Beam Tilted-Head Analytic SPECT Reconstruction: Derivation and Comparison with OSEM, *IEEE Trans. Nucl. Sci.*, vol. 49, pp. 2394-2400, Oct 2002.

- Pieper BC, Bowsher JE, Tornai MP, Peter J, Jaszczak JJ, Breast Tumor Imaging Using Tiltable Head SPECT Cameras,

- Lee T, Braun K, Jazczak J, Bowsher J, Bobkov K, Effects of Lead Shielding of Background Organ Activity in Pinhole SPECT Breast Tumor Imaging, Submitted to the *2004 IEEE Nuclear Science Symposium & Medical Imaging Conference*, 16-21 October, 2004, Rome, Italy.

CONCLUSIONS

From the above research, several conclusions can be drawn. To combat the issue of insufficient sampling, it was shown that an OSEM algorithm will reconstruct the projection data better than a FBP, showing greater SNR and contrast values at all tilt angles. To combat the issues produced by a HAOR, the camera heads were tilted, reducing the radius of rotation and allowing for adequate imaging near the chest wall breast tissue. The combination of an OSEM algorithm and TH-SPECT data offers better shape and uniform activity distribution of the breast, improving contrast and lesion SNR. Concerning the lead shielding, comparison of contrast and SNR between shielded and non-shielded images revealed that contrast and SNR is significantly lower with lead shielding than without lead shielding, the opposite of what we had expected.

In the future, applications of SPECT to breast imaging may provide an alternative method of detecting breast cancer. Future research is required to determine whether an OSEM algorithm can be implemented that can effectively account for inconsistent projection data. Also, future work may include developing more elaborate orbits that provide a complete sampling of the breast, thus meeting the Orlov criteria.

REFERENCES

[1] Pieper BC, Bowsher JE, Tornai MP, Peter J, Greer K, Jaszczak JJ, "Breast Tumor Imaging Using Tiltable Head SPECT Cameras," *IEEE Trans. Nucl. Sci.*, vol. 48, pp. 1477-1482, Aug 2001.,

[2] Orlov SS, "Theory of Three Dimensional Reconstruction," *Sov. Phys. Crystallogr.*, vol. 20, no. 3, pp. 312-314, 1975.

[3] Pieper BC, Bowsher JE, Tornai MP, Archer CN, Jaszczak JJ, "Parallel-Beam Tilted-Head Analytic SPECT Reconstruction: Derivation and Comparison with OSEM," *IEEE Trans. Nucl. Sci.*, vol. 49, pp. 2394-2400, Oct 2002.

[4] Lee T, Braun K, Jazczak J, Bowsher J, Bobkov K, "Effects of Lead Shielding of Background Organ Activity in Pinhole SPECT Breast Tumor Imaging," Submitted to the *2004 IEEE Nuclear Science Symposium & Medical Imaging Conference*, 16-21 October, 2004, Rome, Italy.

APPENDICES

[1] Pieper BC, Bowsher JE, Tornai MP, Peter J, Greer K, Jaszczak JJ, "Breast Tumor Imaging Using Tiltable Head SPECT Cameras," *IEEE Trans. Nucl. Sci.*, vol. 48, pp. 1477-1482, Aug 2001.

[2] Pieper BC, Bowsher JE, Tornai MP, Archer CN, Jaszczak JJ, "Parallel-Beam Tilted-Head Analytic SPECT Reconstruction: Derivation and Comparison with OSEM," *IEEE Trans. Nucl. Sci.*, vol. 49, pp. 2394-2400, Oct 2002.

[3] Lee T, Braun K, Jazczak J, Bowsher J, Bobkov K, "Effects of Lead Shielding of Background Organ Activity in Pinhole SPECT Breast Tumor Imaging," Submitted to the *2004 IEEE Nuclear Science Symposium & Medical Imaging Conference*, 16-21 October, 2004, Rome, Italy.

Breast Tumor Imaging Using a Tiltable Head SPECT Camera

Brett C. Pieper, *Member, IEEE*, James E. Bowsher, *Member, IEEE*, Martin P. Tornai, *Member, IEEE*, Jörg Peter, *Member, IEEE*, Kim Greer, and Ronald J. Jaszczak, *Fellow, IEEE*

Abstract—**As a test bed for dedicated breast single-photon emission computed tomography (SPECT) cameras that are under development, a general purpose SPECT system with two tiltable heads was used to image fillable breast and torso phantoms containing multiple lesions. Breast, liver, and myocardial activity were included in order to simulate direct contamination and Compton scattering expected in clinical scans. The tiltable-head SPECT (TH-SPECT) data were reconstructed using an OS-EM algorithm which accounted for the tilted geometry. High-count planar images were acquired for comparison with TH-SPECT. In order to characterize axial blurring effects inherent with TH-SPECT reconstructions, two cylindrical disk Defrise phantoms, one large Defrise phantom and one mini-Defrise phantom placed inside the fillable breast phantom, were imaged at various tilt angles. Results indicate an increase in axial blurring with greater tilt angle. Reconstructions of the combined fillable breast and torso phantoms containing two 1.15 ml lesions, one centered axially and one proximal to the anterior chest wall within the breast, were most clearly visible in the 30° reconstructed TH-SPECT images, providing lesion signal-to-noise ratio (SNR) and contrast improvements of nearly three times compared to the high-count planar images.**

I. Introduction

FOR BREAST cancer imaging using conventional single-photon emission computed tomography (SPECT) systems, the gamma camera's axis of rotation is parallel to the patient table—a horizontal axis of rotation (HAOR). This geometry decreases breast signals due to torso attenuation and, more importantly, requires a large radius of rotation which yields poor results for SPECT breast imaging [1].

Previous work indicates breast cancer imaging can be improved by using a vertical axis of rotation (VAOR) [1], [2]. In this paper, we expand upon previous VAOR breast imaging by using tiltable gamma cameras. By tilting the camera off axis with respect to the nipple-to-anterior chest axis through the breast, improved imaging of lesions near the chest wall and a reduced radius of rotation (ROR) can be achieved. This paper investigates tilted VAOR breast imaging (see Fig. 1) by simulating a dedicated VAOR system using a HAOR SPECT system with tiltable gamma cameras.

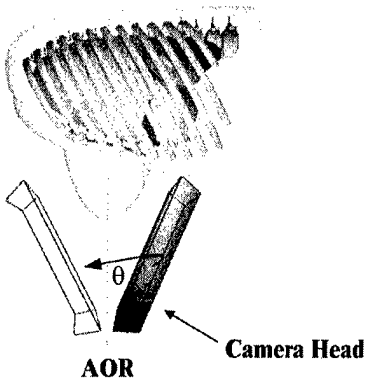

Fig. 1. Schematic of dedicated breast VAOR system.

One major concern with tiltable-head SPECT (TH-SPECT) imaging is insufficient angular sampling. The completeness of reconstructions using TH-SPECT is bound by Orlov sphere conditions [3]. In order to satisfy these conditions, the image space must be sampled over a great circle or equatorial orbit. By tilting the camera heads off axis, this primary requirement is not met (see Fig. 2), and thus there is the potential for artifacts in the reconstructed images. This is also an issue, in general, with slant-hole collimators and rotating slant-hole collimators [4].

Another concern with TH-SPECT imaging is background interference from myocardium, liver, and body tissue that is expected clinically with the use of Tc-99m labeled tracers. By tilting the camera heads off axis, heart and liver activity are introduced into the camera's field of view (FOV) at some projections, potentially contaminating TH-SPECT reconstructions.

II. Materials and Methods

All data were acquired using a tiltable two-headed SPECT system (Vision T-22, Summit Nuclear, Twinsburg, OH) (see Fig. 5). Only one head was used to obtain data during this study. A parallel beam low-energy high-resolution (LEHR) collimator (Hitachi) was used in all experiments. Collimator hole length was 41.0 mm, hexagonal hole size was 1.8 mm, flat-to-flat and septal thickness was 0.18 mm. All images were reconstructed by OS-EM (5 iterations, 8 subsets), with the tilted geometry modeled in the photon detection probabilities. Compton scattering, attenuation, and collimator and crystal spatial resolution were not modeled.

Manuscript received November 12, 2000; revised May 23, 2001. This work was funded by the National Institutes of Health under PHS Grants R01-CA76006 and R01-CA33541, the Whitaker Foundation under Grant RG-99-0305, and the Department of Energy under Grant DE-FG02-96ER62150.

B. C. Pieper is with the Division of Nuclear Medicine, Department of Radiology, Duke University Medical Center, and also with the Department of Biomedical Engineering, Duke University, Durham, NC 27710 USA.

M. P. Tornai and R. J. Jaszczak are with Duke University Medical Center, Durham, NC 27710 USA.

J. Bowsher and K. Greer are with the Division of Nuclear Medicine, Department of Radiology, Duke University Medical Center, Durham, NC 27710 USA.

J. Peter is with the Department of Biophysics and Medical Radiation Physics, German Cancer Research Center, Heidelberg, Germany.

Publisher Item Identifier S 0018-9499(01)08645-2.

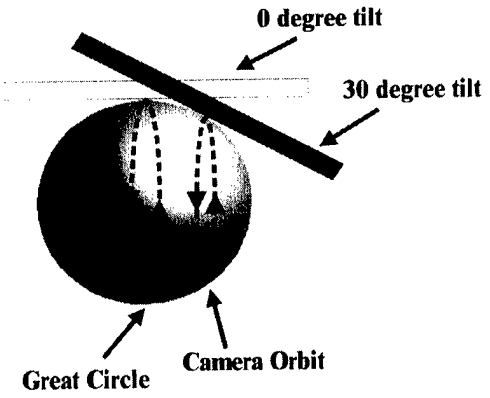

Fig. 2. Sphere showing an equatorial camera orbit and an orbit where the camera head is tilted. The camera is normal and tangential to the sphere at all projection views.

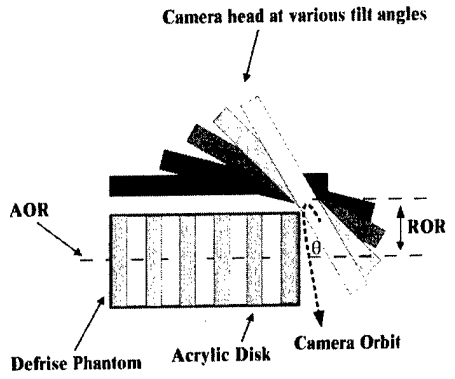

Fig. 3. Schematic of the Defrise phantom with camera head at 0°, 15°, 30°, 45°, and 60° tilt angles. Curved arrow illustrates camera orbit out of page about the AOR.

A. Defrise Disk Phantom

A Defrise disk phantom (see Fig. 3) (Data Spectrum Corp., Hillsborough, NC) was utilized in the first experiment. This phantom consisted of a cylinder containing six acrylic disks placed 1.5 cm apart. The acrylic disks had a thickness of 1.2 cm and a diameter of 18.9 cm. Five emission disks were then formed by adding 16.6 mCi of Tc-99m and water to the cylinder, each hot disk having a uniform concentration of 4.1 μCi/ml. The phantom was then placed parallel to the camera's axis of rotation (AOR) with a radius of rotation (ROR) of 11.5 cm, measured from the center of the camera to the Defirse disk phantom's long axis, perpendicular to the camera's AOR (see Fig. 3). Projection data were taken for 0°, 15°, 30°, 45°, and 60° tilt angles. Each projection data set was acquired for 128 angular views over 360°, and each projection was 128 × 128 pixels and pixel size was 0.48 cm square. Total acquisition time was 7 s per angular step for a total time of 15 minutes. Subsequent acquisition times were increased to compensate for radioactive decay.

B. Breast Phantom with Mini-Disk Phantom

In order to characterize axial blurring within the breast geometry, custom mini-Defrise phantom disks (Data Spectrum Corp., Hillsborough, NC) were placed inside a custom fillable breast phantom (Data Spectrum Corp., Hillsborough, NC) (see Fig. 4). By filling the breast phantom with water having a 22.5 μCi/mL

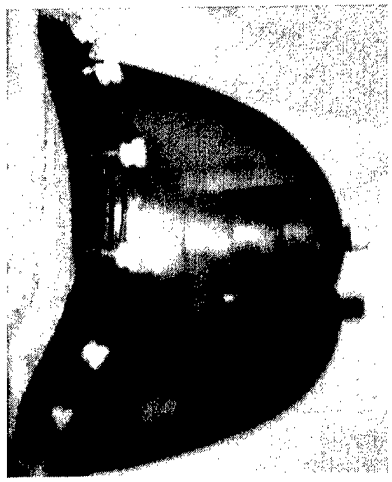

Fig. 4. Photograph of the custom breast phantom with three mini-Defrise disks 8.0 cm in diameter and 1.0 cm thick, separated by a 1.0 cm gap and aligned along the breast axis. Nipple is at right, and curvature at left corresponds with torso shape.

concentration of Tc-99m, three cold disks measuring 1.0 cm in thickness and 8.0 cm in diameter and two hot disks measuring 1.0 cm and 8.0 cm in diameter were formed. The axis of the breast phantom was then placed parallel to the camera's AOR and the radius of rotation was measured from the nipple to the center of the camera, perpendicular to the camera's AOR. Because axial blurring becomes extremely noticeable at larger tilt angles ($> 15°$), projection data were taken for angles of 0°, 5°, 10°, and 15° having RORs of 12.1 cm, 11.8 cm, 11.6 cm, and 10.9 cm respectively. The ROR was decreased with greater tilt angle due to greater access to the breast. Potentially smaller RORs could be possible with dedicated small area breast imaging systems [5]. Total acquisition time was 10 s per angular step or 21.33 min. Subsequent acquisition times were increased to compensate for radioactive decay.

C. Anthropomorphic Torso Phantom and Breast Phantom with Lesions

An anthropomorphic torso phantom (Model ECT/TOR/P, Data Spectrum Corp., Hillsborough, NC) combined with the fillable breast phantom was imaged in this experiment (see Fig. 5) to simulate the expected emission contamination from the myocardium and liver to the specific breast imaging task. The craniocaudal axis of the torso phantom was perpendicular to the camera's axis of rotation, thus necessitating the tilted camera heads and allowing for close proximity imaging of the breast phantom. Two 1.3 cm diameter lesions (1.15 ml) with Tc-99m concentration of 11.1 μCi/ml were suspended inside the left breast. One lesion was placed axially in the center of the breast, 5.1 cm from the nipple. The second lesion was located 2.2 cm anterior to the chest wall and positioned 3.0 cm toward the medial-superior side of the breast. A third 0.9 cm diameter lesion (0.38 ml) with a concentration of 11.1 μCi/ml was placed outside the breast on the chest wall to represent axillary tumor growth. The breast phantom had a uniform concentration of 1.5 μCi/ml. In order simulate contamination effects due to direct superposition of myocardial activity on the breast at some projection views and also Compton scattering expected

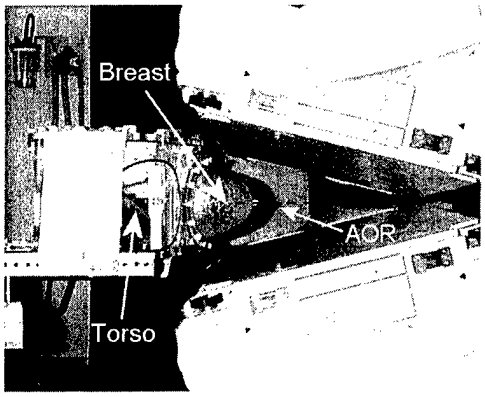

Fig. 5. Photograph of anthropomorphic torso and breast phantoms with dual tilted heads on the SPECT camera.

in clinical scans, the tumor and breast were imaged with additional liver and myocardium activity. The lesion:liver:myocardium:breast-background ratio was 7.4:12.5:12.5:1, giving the liver and heart a Tc-99m concentration of 18.7 μCi/ml.

Projection data were acquired for 0°, 15°, 30°, and 45° tilt angles with ROR's of 18.1 cm, 10.5 cm, 9.4 cm, and 5.9 cm respectively, measured as previously described. The images were acquired for 128 angular views over 360°, and each projection was 128 × 128 pixels and pixel size was 0.48-cm square. Total acquisition time was 32 min, or 15 s per angular step and subsequent acquisition times were increased to compensate for radioactive decay.

Because planar scintimammography is gaining acceptance as an effective way to identify breast lesions greater than 1 cm in diameter [6], a planar scintimammography image (craniocaudal view) was made for comparison. Breast, liver, and myocardium background radiation were present, with the same activity concentration as for TH-SPECT, and the total acquisition time was 5 min.

III. Results

A. Degradative Angular Sampling Effects

Single slice sagittal views of the reconstructed Defrise phantom images at 0°, 15°, 30°, 45°, and 60° are presented in Fig. 6. For the reconstructed sagittal slices, each disk should be regular "bar" shape (see Fig. 6, left, top), but as the tilt angle is increased there is a clear bowing effect in the axial direction which corroborates the results in [7]. The disks are almost unrecognizable in the 30–60° tilts.

Fig. 7 compares the results of the mini-Defrise phantom inserted into the fillable breast phantom. Results from the larger Defrise phantom indicated extreme axial blurring for tilt angles greater than 15°. This experiment investigated smaller tilt angles to evaluate the effects of incomplete sampling with small tilt angles, and also to attempt to minimize the blurring effect but still maximize chest wall imaging without additional orbits to complete the data. A bowing effect similar to that seen in Fig. 6 is clear in these reconstructions, although not as pronounced.

Profiles drawn axially across the left-center of the breast (see Fig. 8) indicate an increase in counts toward the nipple due to the attenuating effects of the Defrise phantom within the breast.

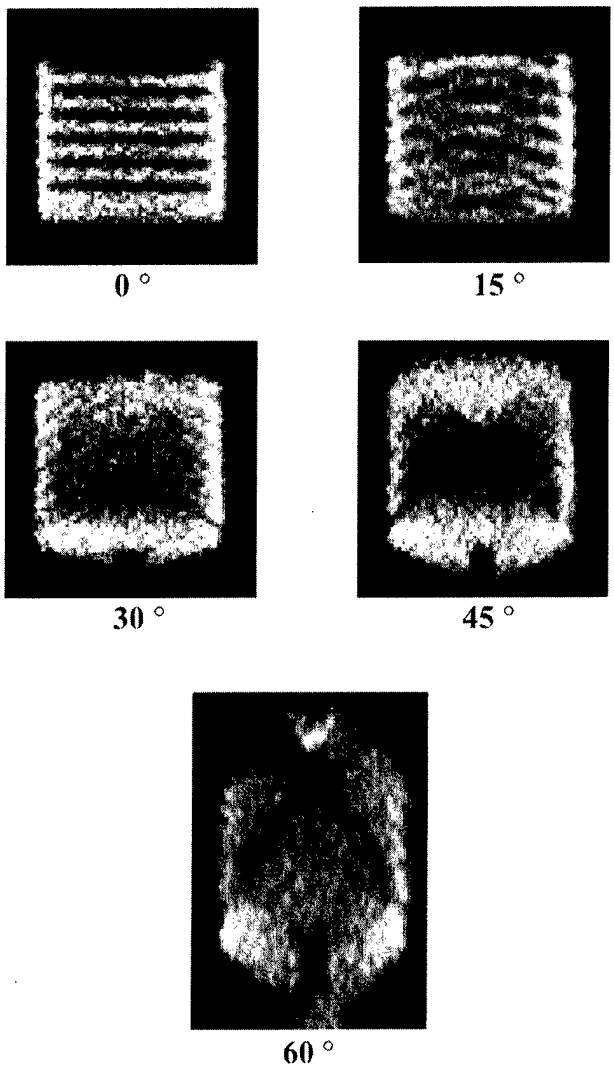

Fig. 6. Single slice sagittal views of OS-EM reconstructed Defrise phantom images at indicated tilt angles.

The profiles also show a definite axial "stretching" effect, as the 15° image is roughly 0.5 cm longer than the 0° image. This result indicates that visualization of axially juxtaposed tumors or shell-like tumors may be difficult to discern.

B. Lesion Imaging with Various Tilt Angles

Reconstructed sagittal views of the fillable breast phantom containing two hot lesions combined with the anthropomorphic torso phantom are presented in Fig. 9 with corresponding profiles at the indicated locations. Background heart, liver, and torso contamination were present, and all profiles were drawn across the center of the lesions. Table I compares the SNR and contrast values for each lesion and tilt angle. Fig. 9 clearly shows an increase in both contrast and SNR as tilt angle is increased from 0° to 30°. Tilt angles beyond 30° do not significantly improve either contrast or SNR values.

The third lesion, attached to the anthropomorphic torso phantom anterior to the chest wall and superior to the left breast, was also reconstructed. Although not shown, the lesion is clearly visible in all reconstructions.

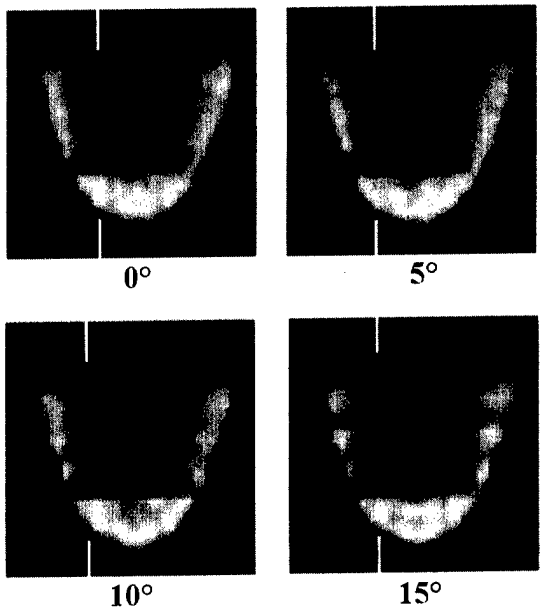

Fig. 7. Single slice sagittal view OS-EM reconstructions of mini-Defrise phantom combined with fillable breast phantom at indicated angles. Profile markers are drawn axially across left-center of breast phantom.

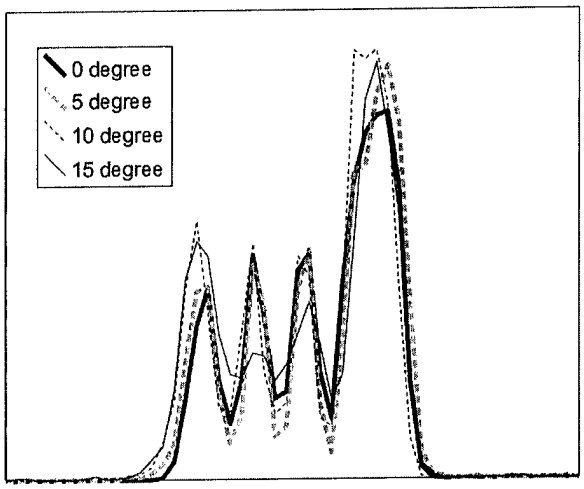

Fig. 8. Profiles drawn across single slice sagittal views of mini-Defrise phantom (see Fig. 7). Left corresponds to bottom portion of the images shown in Fig. 7. Camera head was tilted away from chest wall. Note increase in breast's axial length with greater tilt angle.

IV. Discussion and Conclusion

Because of insufficient sampling, axial blurring is evident in all TH-SPECT reconstructions. As shown with the larger Defrise phantom, large tilt angles (45° and 60°) yield extremely distorted images. Because the ROR can be decreased as tilt angle is increased, it is important to find an acceptable combination between the two, specifically one which minimizes axial blurring effects while still maximizing SNR and contrast values. Tradeoffs between higher resolution parallel hole collimators versus higher sensitivity collimators should be considered. The use of nonparallel hole collimators should also be considered in this application since these geometries could potentially help complete undersampled regions of the Orlov sphere [8].

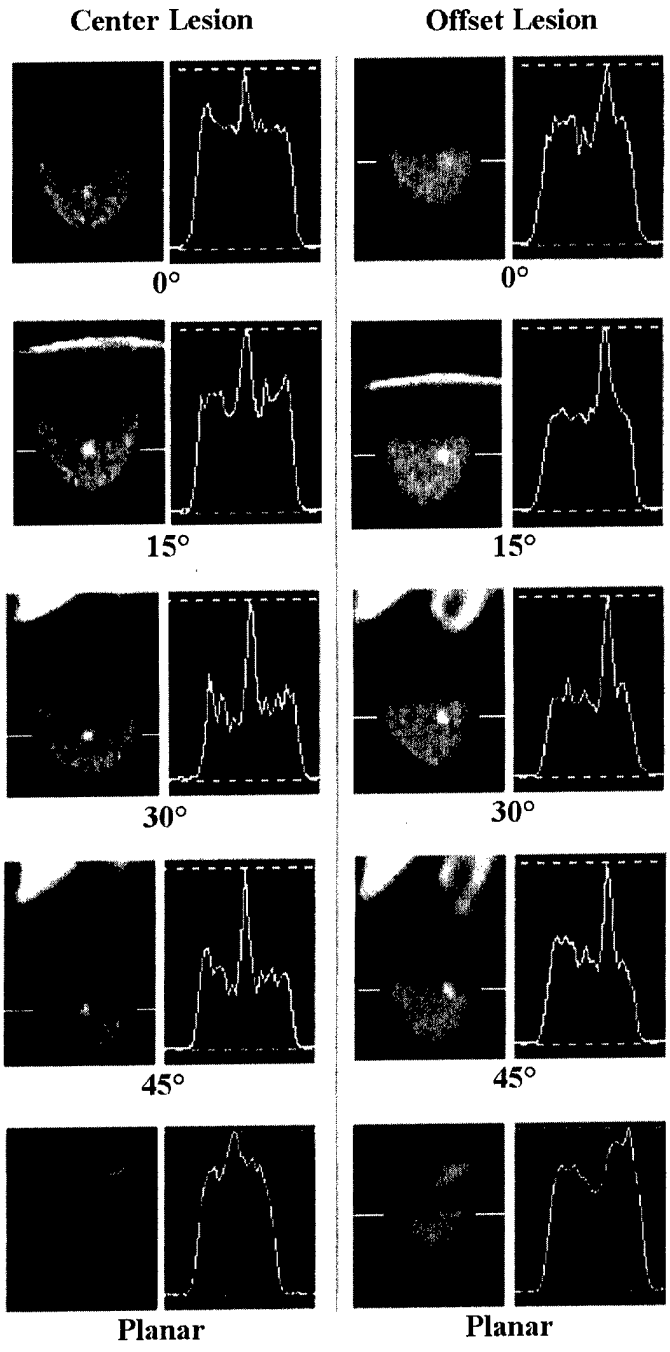

Fig. 9. Sagittal view reconstructions of fillable breast phantom attached to anthropomorphic torso phantom containing two hot lesions (one lesion axially centered, one lesion anterior to the chest wall and positioned toward the medial-superior side of the breast) at 0°, 15°, 30°, and 45° tilt angles as well as conventional high-count planar images. Profiles for each lesion are also shown. The cold spot directly behind the central lesion is the acrylic support used to hold lesion in place and the cold gap between the breast and torso represents phantom chest wall.

As Fig. 9 shows, larger tilt angles can "stretch" the breast axially. This stretching phenomenon also affects the lesion, and can potentially blur together axially offset lesions or distort shell-like lesions. This phenomenon has very little effect, however, on the 15° degree reconstruction. Compared to the 0° reconstruction which has no distortions, SNR and contrast values between the two are significantly different,

TABLE I
SNR AND CONTRAST VALUES FOR CENTER LESION AND OFFSET LESION AT 0°, 15°, 30°, AND 45° TILT ANGLES AS WELL AS A CONVENTIONAL HIGH-COUNT PLANAR IMAGE (CRANIOCAUDAL VIEW)

	SNR $[(\mu_{lesion} - \mu_{breast})/\sigma_{breast}]$	Contrast $[(\mu_{lesion} - \mu_{breast})/\mu_{breast}]$	ROR (cm)
Center lesion			
Planar	2.10	0.20	18.1
0°	2.09	0.25	18.1
15°	3.56	0.49	10.5
30°	4.89	0.59	9.4
45°	5.15	0.59	5.9
Offset lesion			
Planar	2.04	0.20	18.1
0°	2.13	0.24	18.1
15°	3.74	0.51	10.5
30°	6.32	0.63	9.4
45°	5.16	0.49	5.9

providing lesion SNR and contrast improvements of up to two times for the center lesion (Table I). Although 30° and 45° tilt reconstructions have even better SNR and contrast values, distortions of the breast are much more evident, compared to the smaller tilt angles.

As Table I indicates, effective radius of rotation significantly decreases as tilt angle is increased. Although the 45° radius of rotation was almost half that of the 30°, extreme insufficient sampling as well as attenuation prevented further contrast and SNR improvements. Less dramatic decreases in ROR due to increasing tilt angle would be achieved using a small-area dedicated breast SPECT system [5], although results indicate SNR and contrast values should improve with any reduction of ROR. In addition to viewing lesions near the torso-breast interface, TH-SPECT reconstructions may considerably improve SNR and contrast values even for lesions within the breast, presumably by allowing for a reduced ROR. Localization of the lesion, however, may be difficult with the present artifacts.

The blurring and distortion artifacts become more apparent with greater axial nonuniformity in the breast, as shown in Fig. 7 with the mini-Defrise phantom. The 15° tilt reconstruction of the mini-Defrise phantom inside the fillable breast phantom highlights a definite bowing effect. These results indicate that artifacts will be more present when objects are axially aligned and imaged with a TH-SPECT technique. This bowing effect is not visualized in Fig. 9 reconstructions simply due to the uniformity of breast tissue and spherical lesions. Nonuniform breast lesions, such as distorted or shell-like tumors, may result in further image degradation even at small angular tilts. Although dedicated breast SPECT systems under development may also suffer from the artifacts illustrated in this study, those systems may further provide SNR and contrast improvements due to reduced RORs [5].

When the reconstruction was limited to the breast only, essentially eliminating background interference from the FOV, a cupping artifact [9] was present. This cupping artifact is an artificial increase in activity near the edge of the FOV. By reconstructing the entire image space (heart and liver interference included), this artifact was eliminated [9]. It remains to be seen if small-area dedicated breast SPECT systems will suffer from these limitations and if reconstructed images from a small-area camera contain the cupping artifact.

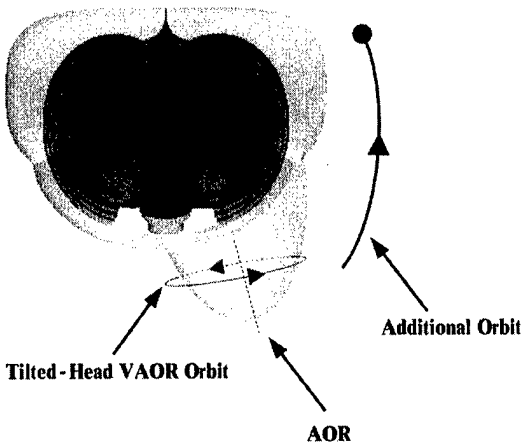

Fig. 10. Transverse view of phantom illustrating TH-SPECT acquisition as well as an additional HAOR orbit to gather insufficiently sampled data.

Possible modifications can be made to the TH-SPECT geometry to account for insufficient sampling and to reduce, if not eliminate, axial blurring artifacts. Because Orlov Sphere requirements are not met with any degree of camera tilt [3], an additional orbit is required to satisfy these conditions for fully quantitative SPECT imaging. Fig. 10 introduces one such additional orbit. If TH-SPECT VAOR data is collected and combined with an incomplete HAOR orbit [10], Orlov Sphere requirements should be met and blurring due to insufficient axial sampling should be eliminated. This short arc-orbit (ranging from 10° to 90° depending upon tilt angle) needs only to gather enough data to fully sample the breast, as accurate heart and liver reconstruction may not be necessary.

ACKNOWLEDGMENT

The authors would like to thank Duke Medical Center for the use of the gamma camera, and N. Jaszczak and Data Spectrum Corporation for use of phantoms.

REFERENCES

[1] H. Wang, C. Scarfone, K. L. Greer, R. E. Coleman, and R. J. Jaszczak, "Prone breast tumor imaging using vertical axis-of-rotation (VAOR) SPECT systems: An initial study," *IEEE Trans. Nucl. Sci.*, vol. 44, pp. 1271–1276, June 1997.

[2] M. P. Tornai, B. C. Pieper, J. E. Bowsher, and R. J. Jaszczak, "Effects of pinhole material and aperture size on lesion contrast and SNR breast SPECT," in Conf. Rec. IEEE Nuclear Science Symp. Medical Imaging Conf., 2000, submitted for publication.

[3] S. S. Orlov, "Theory of three dimensional reconstruction," *Kristallografiya*, vol. 20, pp. 511–515, May–June 1975.

[4] D. E. Wessell, "Rotating slant-hole single-photon emission-computed tomography," *Med. Phys.*, vol. 27, no. 7, p. 1697, 2000.

[5] M. P. Tornai, J. E. Bowsher, C. N. Archer, J. Peter, L. R. MacDonald, B. E. Patt, J. S. Iwanczyk, R. J. Jaszczak, and R. E. Coleman, "Dedicated breast imaging with an ASET: Application specific emission tomograph," *J. Nucl. Med.*, vol. 42, no. 5, p. 97, 2001.

[6] I. Khalkali, J. A. Cutrone, I. G. Mena, L. E. Diggles, R. J. Venegas, H. I. Vargas, B. L. Jackson, S. Khalkali, J. F. Moss, and S. R. Klein, "Scintimammography: The complementary role of Tc-99m sestamibi prone breast imaging for the diagnosis of breast carcinoma," *Radiology*, vol. 336, pp. 1784–1789, 1995.

[7] C. D. Stone, M. F. Smith, K. L. Greer, and R. J. Jaszczak, "A combined half-cone beam and parallel hole collimation," *IEEE Trans. Nucl. Sci.*, vol. 45, pp. 1219–1224, June 1998.

[8] J. Li, R. J. Jaszczak, K. L. Greer, R. E. Coleman, Z. Cao, and B. M. W. Tsui, "Direct cone beam SPECT reconstruction with camera tilt," *Phys. Med. Biol.*, vol. 38, pp. 241–258, 1993.

[9] M. A. King, D. Luo, S. T. Dahlberg, and B. J. Villegas, "Transmission imaging of large attenuators using a slant hole collimator on a three-headed SPECT system," *Med. Phys.*, vol. 23, no. 3, pp. 263–271, 1996.

[10] S. Metzler, J. E. Bowsher, M. P. Tornai, B. C. Pieper, and R. J. Jaszczak, "SPECT breast imaging combing horizontal and vertical axes of rotation," IEEE Trans. Nucl. Sci., to be published.

Parallel-Beam Tilted-Head Analytic SPECT Reconstruction: Derivation and Comparison With OSEM

Brett C. Pieper, *Member, IEEE*, James E. Bowsher, *Member, IEEE*, Martin P. Tornai, *Member, IEEE*, Caryl N. Archer, *Member, IEEE*, and Ronald J. Jaszczak, *Fellow, IEEE*

Abstract—**Parallel-beam tilted-head single photon emission computed tomography (TH-SPECT) was previously implemented on a SPECT system for its potential to image breast lesions and nearby axilla of seated, upright women. All TH-SPECT reconstructions will contain artifacts since the tilted orbit does not satisfy the Orlov sampling criteria. However, it is not clear which reconstruction method, if any, is better suited for TH-SPECT data. Here a geometric derivation of the ramp filter for tilted parallel-beam geometries is presented. A filtered backprojection (FBP) algorithm, using this filter, was then implemented and compared with an iterative ordered subsets expectation maximization (OSEM) algorithm, using TH-SPECT data. A breast scan at various tilt angles was simulated and used to generate a noise versus bias study for both methods. Contrast and signal-to-noise ratio (SNR) values, as well as axial elongation present in all TH-SPECT reconstructions, were characterized using a mini-Defrise disk phantom placed inside a fillable breast phantom and imaged from 0 to 15° head tilt. A fillable breast phantom containing lesions was also imaged with a system dedicated to prone breast SPECT from 0 to 30° to evaluate the effects of incomplete sampling due to greater tilt angles. FBP noise versus bias studies indicated a greater increase in bias with tilt angle compared to OSEM reconstructions. At small tilt angles about the mini-Defrise disk phantom, poorer contrasts were obtained with FBP compared to OSEM at similar noise levels. All reconstructions of the fillable breast phantom indicated axial elongation at greater tilt angles, although FBP reconstructions displayed an increase in stretching distortions of the breast. OSEM SNR and contrast values were higher at all degrees of tilt. In conclusion, measured results indicate OSEM TH-SPECT reconstruction provides better contrast and SNR values and may offer better shape and uniform activity distribution of the breast compared to FBP methods.**

Index Terms—**Breast imaging, filtered backprojection (FBP), ordered subsets expectation maximization (OSEM), Orlov, single photon emission computed tomography (SPECT).**

I. Introduction

TILTED-HEAD single photon emission computed tomography (TH-SPECT) parallel-beam imaging of breast lesions has been shown to offer superior lesion contrast and signal-to-noise ratio (SNR) values compared to conventional SPECT geometries [1]. Reconstruction of TH-SPECT data requires a three-dimensional reconstruction algorithm. Iterative methods have thus far been used to accurately model the complex (albeit incomplete) sampling of frequency space associated with the tilted circular orbit. It may be useful, however, to reconstruct TH-SPECT data using analytic filtered backprojection (FBP) methods given the speed and linearity associated with such methods.

Conventional two-dimensional (2-D) FBP SPECT reconstruction for parallel-beam collimation relies on the standard one-dimensional ramp filter. This ramp filter has also been shown to be the backprojection filter for three–dimensional (3-D) tilted parallel-beam geometries [2]. Due to insufficient Orlov Sphere sampling [3], TH-SPECT acquisitions introduce a null space of unmeasured frequency components whose frequency-space volume is dependent upon tilt angle. These unmeasured frequency components may have negative effects on image reconstruction. One such effect is axial stretching which produces unwanted distortion of the patient's body contour [1]. Another related effect is inaccurate activity distribution specifically due to insufficient sampling of the Orlov Sphere. With these negative effects in mind, it is unclear which image reconstruction method is better suited for TH-SPECT data. This paper develops a geometric derivation of the ramp filter for TH-SPECT and then compares parallel-beam TH-SPECT FBP reconstruction with an existing iterative ordered subsets expectation maximization (OSEM) algorithm [1], [4]. Simulation studies as well as phantom studies are performed and evaluated.

Manuscript received November 5, 2001; revised July 29, 2002. This work was supported by Grant DAMD17-01-1-0226 from the Department of Defense, PHS Grants R01-CA76006 and R01-CA33541 from the National Institutes of Health, Grant RG-99-0305 from the Whitaker Foundation, and Grant DE-FG02-96ER62150 from the Department of Energy.

B. C. Pieper, M. P. Tornai, C. N. Archer, and R. J. Jaszczak are with the Department of Biomedical Engineering, Duke University, Durham, NC 27710 USA, and also with the Department of Radiology, Duke University Medical Center, Durham, NC 27710 USA (e-mail: pieper@dec3.mc.duke.edu; martin.tornai@duke.edu; cnb3@duke.edu; rjj@dec3.mc.duke.edu).

J. E. Bowsher is with the Department of Radiology, Duke University Medical Center, Durham, NC 27710 USA (e-mail: jeb@dec3.mc.duke.edu).

Digital Object Identifier 10.1109/TNS.2002.803781

II. Methods

A. TH-SPECT Reconstruction

Three spatial domain coordinate systems are used (Fig. 1) and are defined as (x, y, z), (x', y', z'), and (x'', y'', z''). The object is expressed within the fixed (x, y, z) coordinate system as $f(x, y, z)$. The (x', y', z') system is a rotational coordinate system rotated about the z axis by angle θ. The third coordinate system (x'', y'', z'') represents the tilt of the (x', y', z') system about the y' axis by tilt angle ϕ. The object's frequency domain representation is expressed within the fixed (μ, ν, τ) system as $F(\mu, \nu, \tau)$, and rotations within this system are similarly defined as (μ', ν', τ'), and (μ'', ν'', τ'').

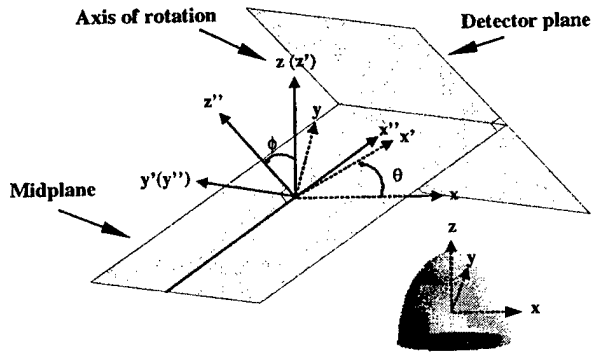

Fig. 1. Illustration of tilted geometry and (x, y, z) coordinate system. Lower-right illustration indicates breast positioning within the tilted geometry, where the z axis passes through the nipple and the center of the base of the breast. Dashed lines indicate axis is behind object.

Rotation of (x, y, z), or similarly (μ, ν, τ), by angle θ produces the following transformations:

$$\begin{aligned} x' &= x\cos\theta + y\sin\theta \\ y' &= -x\sin\theta + y\cos\theta \\ z' &= z. \end{aligned} \tag{1}$$

Likewise, rotation of (x', y', z'), or similarly (μ', ν', τ'), by angle ϕ produces the following transformations:

$$\begin{aligned} x'' &= x\cos\theta\cos\phi + y\sin\theta\cos\phi - z\sin\phi \\ y'' &= -x\sin\theta + y\cos\theta \\ z'' &= x\cos\theta\sin\phi + y\sin\theta\sin\phi + z\cos\phi. \end{aligned} \tag{2}$$

1) Backprojection Filter for Non-Tilted Parallel-Beam Geometry: In order to suggest a filter for TH-SPECT data, we first examine filtering for nontilted parallel-beam geometries. The Fourier projection-slice theorem implies that by taking projections at multiple angles θ with $\phi = 0$, values of $F(\mu, \nu, \tau)$ will be known along radial planes centered at the origin and perpendicular to the projections [5]–[10]. Fig. 2 (top) illustrates the frequency domain representation of a single nontilted projection at angle θ, with ω being the distance from one arbitrary sample point to the axis of rotation (AOR) τ. Rotation about τ fills $F(\mu, \nu, \tau)$ with multiple circles of discrete sample points. Fig. 2 (bottom) illustrates a slice at a constant value of τ. As the radial distance ω increases, the density of sample points within a given rotation circle decreases. Specifically, the density of sample points within each circle is directly proportional to $1/\omega$, the inverse of the circles' circumference, or, in our rotated coordinate system, $1/\nu''$. Because the distance γ between all rotation circles is constant, the density of circles within the plane is also constant. The density of sample points, which can be expressed as the density of circles times the density of points per circle, is therefore proportional to $1/\omega$. The filter ω, which is the well-known ramp filter, compensates for this varying sampling density. Because lower frequencies are sampled more densely than higher frequencies, a filter is needed to correct for this difference in sampling. Because each slice along τ is identical in sample density, the backprojection filter for nontilted parallel-beam data is one-dimensional across projections.

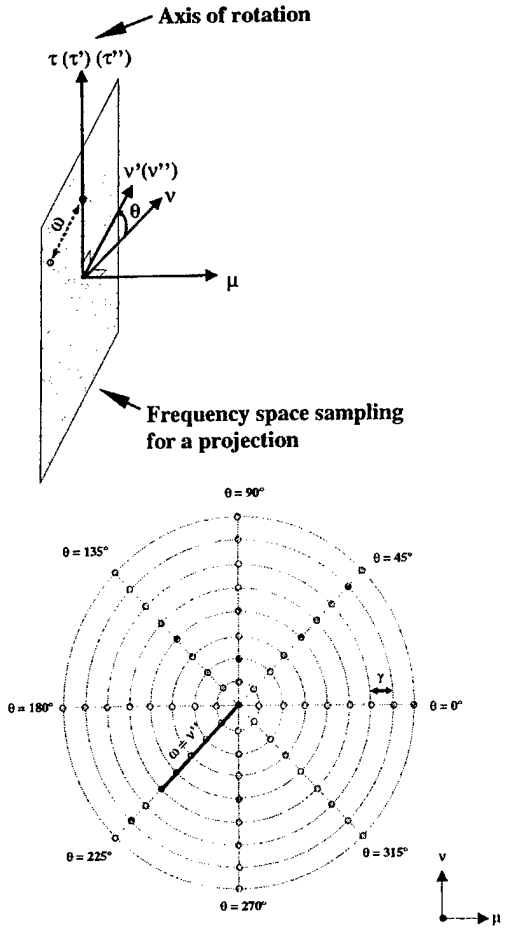

Fig. 2. (Top) Illustration of Fourier projection-slice theorem for nontilted data. The plane indicates the frequencies sampled by a projection at angle θ. ω represents the distance between an arbitrary sample point and the τ axis. (Bottom) Frequency domain slice at a constant value of τ showing the discrete sample points at distances $\nu'' = \nu' = \omega$ from the AOR and rotated by θ. Distance γ represents the constant distance between circles of discrete sample points.

2) Backprojection Filter for Tilted Parallel-Beam Geometry: For tilted parallel-beam data ($\phi \neq 0$), Fig. 3 (top) illustrates the region of frequency space sampled by a projection at angles θ and ϕ. The distance ω from the axis of rotation τ to a sample point is $\omega = \sqrt{\nu''^2 + \tau''^2 \sin^2\phi}$.

Sampled frequencies correspond to discrete values of ν'', and each value of ν'' lies on a circle of sample points having a radius ω, with one sample point per angle θ. The density of points along a given circle is inversely proportional to the circles' radius, that is, proportional to

$$\frac{1}{\sqrt{\nu''^2 + \tau''^2\sin^2\phi}}. \tag{3}$$

In contrast to nontilted data, the distance γ between circles in this plane is not constant but rather depends upon ν'' and τ'' (Fig. 3, bottom). The density of circles is proportional to the reciprocal of the distance between circles, that is, proportional to

$$\frac{d\nu''}{d\omega} = \frac{\sqrt{\nu''^2 + \tau''^2\sin^2\phi}}{|\nu''|}. \tag{4}$$

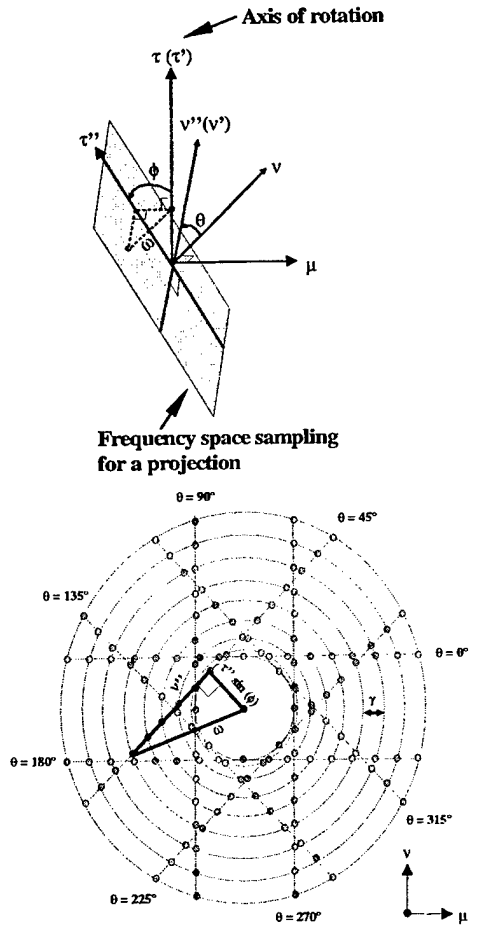

Fig. 3. (Top) Illustration of Fourier projection-slice theorem for tilted data. Plane illustrates the frequency space sampling for a projection at angles θ and ϕ. ω represents distance between arbitrary sample point and the τ axis. (Bottom) Frequency domain slice at constant value $\tau \neq 0$ built up from discrete sample points along ν'' and over rotation angles θ. Frequencies are not measured within the concentric, inner circle of radius of $\tau'' \sin \phi$. Unmeasured frequency region decreases as $\tau \rightarrow 0$ and becomes Fig. 2 (bottom) when $\tau = 0$. Note distance ω is now a function of both ν'' and $\tau'' \sin \phi$. Distance γ represents the distance between circles built up from discrete sample points. Note circles are more dense near $\omega = \tau'' \sin \phi$ and less dense with increasing ω. For simplicity, sample points were only shown at 45–degree increments. Conventional, finer sampling would diminish this nonuniform density appearance within each circle.

As ν'' increases, the distance between neighboring circles increases. These circles are more dense near $\omega = \tau'' \sin \phi$ than at higher ω. For $\omega < |\tau'' \sin \phi|$, the density of sample points within the plane is zero. For $w \geq |\tau'' \sin \phi|$, the density of sample points within the plane is the product of (3) and (4), which is $1/|\nu''|$.

Finally, because the spacing of sample points in the τ direction for tilted data is constant, although compressed, a third constant component, $1/\cos\phi$, can be included.

Multiplying these three density components yields

$$\frac{1}{\sqrt{\nu''^2 + \tau''^2 \sin^2\phi}} \cdot \frac{\sqrt{\nu''^2 + \tau''^2 \sin^2\phi}}{|\nu''|} \cdot \frac{1}{\cos\phi} = \frac{1}{|\nu''| \cos\phi} \tag{5}$$

for the density of all points when $\omega \geq |\tau'' \sin \phi|$. This density is the modulation transfer function (MTF) of the ideal (no attenuation, perfect spatial resolution) tilted parallel-beam measurement. For $\omega < |\tau'' \sin \phi|$, the MTF is zero, so those frequencies

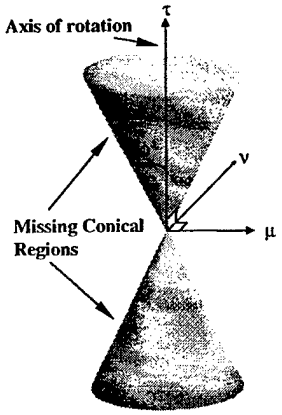

Fig. 4. Illustration of missing conical regions present in all TH-SPECT frequency space representations. Volume of missing region increases with tilt angle ϕ.

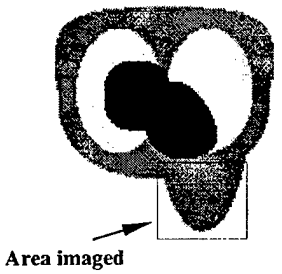

Fig. 5. Transverse view of digital anthropomorphic Peter phantom. Squared breast region indicates the subsection of phantom which was imaged.

cannot be recovered. These frequencies can be represented as missing conical regions whose volumes increase with tilt angle ϕ (Fig. 4).

For $\omega \geq |\tau'' \sin \phi|$, (5) indicates that the MTF can be inverted by the scaled ramp filter, $|\nu'' \cos \phi|$. This geometrical derivation is consistent with previous derivations of the back-projection filter for the tilted parallel-beam geometry [2].

B. Simulated Breast Scan

In order to compare OSEM and FBP for tilted parallel-beam breast imaging, a vertical axis of rotation (VAOR) scan was simulated using a section of the digital anthropomorphic Peter phantom [11]. This computer phantom consists of various volumetric regions in the torso (Fig. 5). For this study, only the left breast (11 cm base-to-nipple, 14 cm base diameter) containing a uniform activity concentration was scanned and no torso activity was present. The phantom was implemented on a 168 × 168 × 168 grid, voxels 0.35 cm on a side. The camera's AOR coincided with a line from the base of the breast through the nipple (Fig. 6). The simulated VAOR scan used a 22.4 × 22.4 cm field-of-view (FOV) parallel-hole gamma camera, and each projection data set was acquired for 128 angular views over 360°. Each projection was 64 × 64 pixels and pixel size was 0.35 cm^2. Projection data were simulated for 0°, 15°, 30°, and 45° tilt angles. Expected values for VAOR projection data were analytically computed based on forward projections of activity within the breast region only. Compton scattering, attenuation, and collimator and crystal spatial resolution were not modeled.

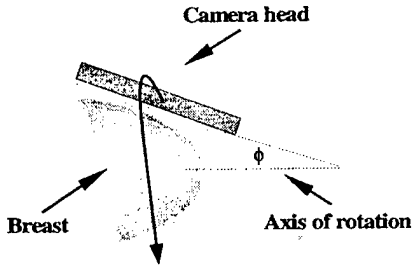

Fig. 6. Illustration of simulated breast scan. Breast represents subsection of digital anthropomorphic Peter phantom and ϕ represents angular camera tilt.

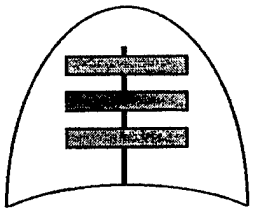

Fig. 7. Schematic of breast phantom with three mini-Defrise disks. Nipple is at top and curvature at bottom corresponds to torso shape.

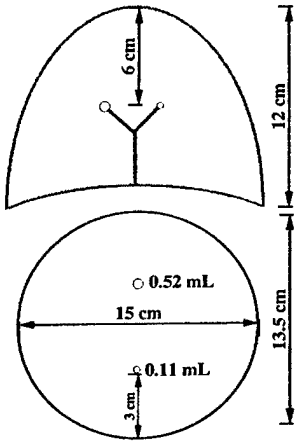

Fig. 8. Schematic of 950 ml breast phantom containing lesions. Large lesion is located at a superior medial aspect of the breast, 6 cm from nipple and 3 cm from a normal to the surface of the breast. Smaller lesion is located at an inferior medial aspect of the breast, 6 cm from nipple and 3 cm from a normal surface of the breast (top schematic shows relative height and lesion displacement; Bottom schematic illustrates actual lesion orientation in the breast).

An ensemble study was generated consisting of 50 acquisitions per tilt angle and based on Poisson variation about the expected values. OSEM reconstructions were performed with the tilted geometry modeled in the photon detection probabilities, and noise and bias values were computed for 1–50 iterations (eight subsets). Reconstructed OSEM images were 32 × 32 × 32 cubic voxels each, 0.7-cm wide. Compton scattering, attenuation, and collimator and crystal spatial resolution were not modeled within the reconstruction. FBP reconstruction was similarly performed with images also 32 × 32 × 32 cubic voxels, 0.7-cm wide. FBP images were post-filtered using a 3-D Butterworth filter. Butterworth filter cut-off frequencies, the frequencies at which the gain equals 0.707, ranged from 0.1–1.0 cycles/pixel with frequency order equal to 10.

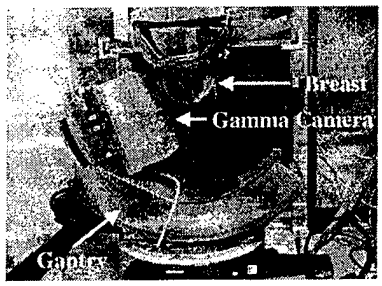

Fig. 9. Photograph of fillable breast phantom suspended over the ASET system.

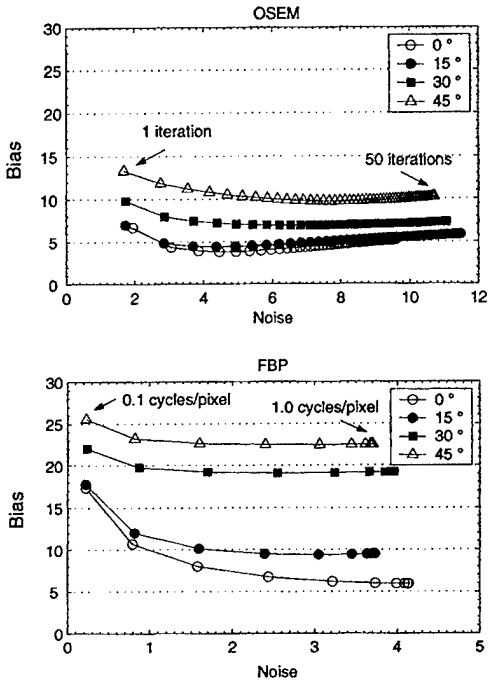

Fig. 10. Noise versus bias plots for OSEM (top) and FBP (bottom) reconstructions of simulated breast scan at 0°, 15°, 30°, and 45° tilt. OSEM data points correspond to iterations 1-50 in increments of one iteration from left to right. FBP data points indicate Butterworth filter cutoffs (1.0 to 0.1 cycles/pixel in increments of 0.1 cycles/pixel from right to left, where furthest right point indicates no post-filtering). OSEM yielded the lower bias for similar noise values.

Noise versus bias curves were generated for both OSEM and FBP reconstructions. Noise was computed as the standard deviation over the ensemble on a pixel-by-pixel basis. Bias was defined as $\sqrt{\sum_{i=1}^{N}(\overline{x}_i - x_i^{(t)})^2}$, where N is the number of voxels, $\overline{x}_i$ is the ith pixel value of the average image, and $x_i^{(t)}$ is the value of the ith pixel in the true phantom image.

C. Defrise Disk Phantom Scan

Mini-Defrise phantom disks (Data Spectrum Corp., Hillsborough, NC) were placed inside a fillable breast phantom (Model ECT/FL BR/A, Data Spectrum Corp., Hillsborough, NC) (Fig. 7). Data were acquired using one head of a tiltable two headed SPECT system (Vision T-22, Summit Nuclear, Twinsburg, OH) and a parallel beam low energy high resolution (LEHR) collimator (Hitachi, Tokyo, Japan) (hole length = 41.0 mm, flat to flat hexagonal hole size = 1.8 mm, septal

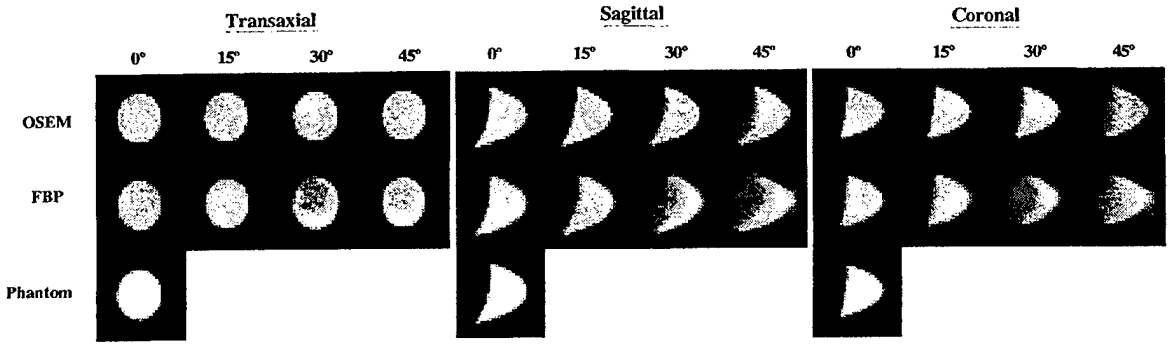

Fig. 11. Transaxial, coronal, and sagittal (with respect to the breast reference frame) OSEM and FBP reconstruction slices for simulated breast scan. Slices were taken for 0°, 15°, 30°, and 45° tilt and corresponding truth phantom slices located at bottom.

thickness = 0.18 mm). The breast phantom contained three cold Defrise-phantom disks measuring 1.0 cm in thickness and 8.0 cm in diameter and with a 1.0-cm gap between disks. The breast phantom was filled with water having a 22.5 μCi/ml concentration of Tc-99m. The axis of the breast phantom was then aligned parallel to the camera's AOR through the nipple, and the radius of rotation (ROR) was measured perpendicular to the center of the camera and to the nipple. Projection data were acquired for tilt angles of 0°, 5°, 10°, and 15° having RORs of 12.1 cm, 11.8 cm, 11.4 cm, and 10.5 cm, respectively. The ROR decreased with greater tilt angle due to greater access to the breast. Total acquisition time was 10 s per angular step or 21.33 min over 360°. Acquisition times were adjusted to compensate for radioactive decay.

OSEM (eight subsets, three iterations) and FBP (Butterworth filtered, cut-off = 0.5 cycles/cm, order = 10) reconstructions were performed for all tilt angles, and final images were 128 × 128 × 128 cubic voxels, 0.48 cm on a side. Iteration and filter parameters were determined from aforementioned noise versus bias study.

D. Fillable Breast Phantom With Lesions

The fillable breast phantom (950 ml) containing two spherical lesions, 1.0 cm diameter (0.52 ml) and 0.6 cm diameter (0.11 ml) (models ECT/HOL-468/A, Data Spectrum Corp., Hillsborough, NC), was also imaged in this experiment (Fig. 8). Data were acquired using a <13 × 13 cm FOV LumaGEM™ gamma camera (Gamma Medica, Inc., Northridge, CA) (hole length = 23.6 mm, flat to flat hexagonal hole size = 1.22 mm, septal thickness = 0.2 mm) as a component on a dedicated Application Specific Emission Tomograph (ASET) gantry [12] (Fig. 9). The breast phantom contained ^{99m}Tc-pertechnetate (140.6 keV) activity and water and lesions : breast activity concentration was 5.94 : 1. Images were acquired for 128 angular views over 360°, and each projection was 54 × 54 pixels, each 2.2 mm^2. Total acquisition time was 20 min, or 9.375 s per angular step. Projection data were acquired for 0°, 10°, 20°, and 30° tilt angles with RORs of 7.47 cm, 6.63 cm, 5.48 cm, and 5.48 cm, respectively, measured from the camera head to the center-of-rotation point. Greater tilted angles allow for the smaller RORs.

OSEM (eight subsets, three iterations) and FBP (Butterworth filtered, cut-off = 0.5 cycles/cm, order = 10) reconstructions were performed for all tilt angles, and final images were 54 × 54 × 54 cubic voxels, 0.22 cm on a side. Iteration and filter parameters were determined from aforementioned noise versus bias study to provide similar noise levels for both methods.

For both reconstruction methods at all degrees of tilt, an elliptical, 11 pixel region-of-interest (ROI) was taken for the large lesion and a similar 121-pixel ROI was taken in the breast. Lesion contrast was calculated as $(\mu_{lesion} - \mu_{breast})/\mu_{breast}$, and SNR as $(\mu_{lesion} - \mu_{breast})/\sigma_{breast}$, where μ = mean and σ = standard deviation of selected ROIs.

III. Results

A. Simulated Breast Scan

Fig. 10 presents noise versus bias plots for OSEM and FBP reconstructions of the simulated breast scan. Fig. 11 presents transaxial, sagittal, and coronal mid-slices (with respect to the breast reference frame) for FBP (no post-filtering), and OSEM (3 iterations) reconstruction methods at 0°, 15°, 30°, and 45°. Iteration cut-offs were chosen to provide approximately equal noise for both reconstruction methods. FBP results indicate a greater increase in backprojection artifacts with greater angular tilt. OSEM reconstructions were better able to maintain a clear, defined border around the breast, but both methods displayed some degree of axial stretching of the breast as well as inaccurate activity distribution with greater tilt. Stretching effects were not found transaxially, however, due to complete frequency sampling of the $\tau = 0$ plane (Fig. 3). This is consistent with tilted cone-beam reconstruction [13], [14], where distortions were most pronounced along the direction parallel to the rotation axis but not along the transverse direction. Ideally, the breast would be fully angularly sampled to satisfy the Orlov condition, and hence reduce currently observed elongation and object distortion artifacts [1], [4].

FBP noise versus bias plots indicate greater bias with tilt angle compared to OSEM reconstructions (Fig. 10). A 50% increase in bias was noted between FBP 0° and 15° recontructions, while only a 15% increase in bias was noted between OSEM 0° and 15° reconstructions, compared at similar noise levels. Butterworth filtering tended to offer the best compromise between noise and bias for FBP reconstructions, specifically at a 0.3 cycles/pixel cutoff. Three iterations displayed the

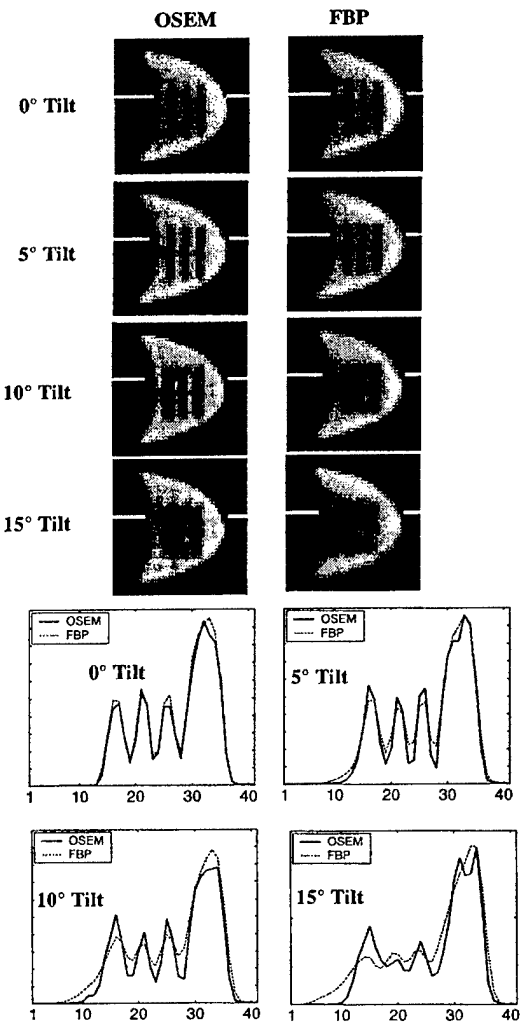

Fig. 12. Sagittal view OSEM and FBP reconstructions of mini-Defrise phantom combined with fillable breast phantom and corresponding profiles. Profile markers are drawn axially across left-center of breast phantom.

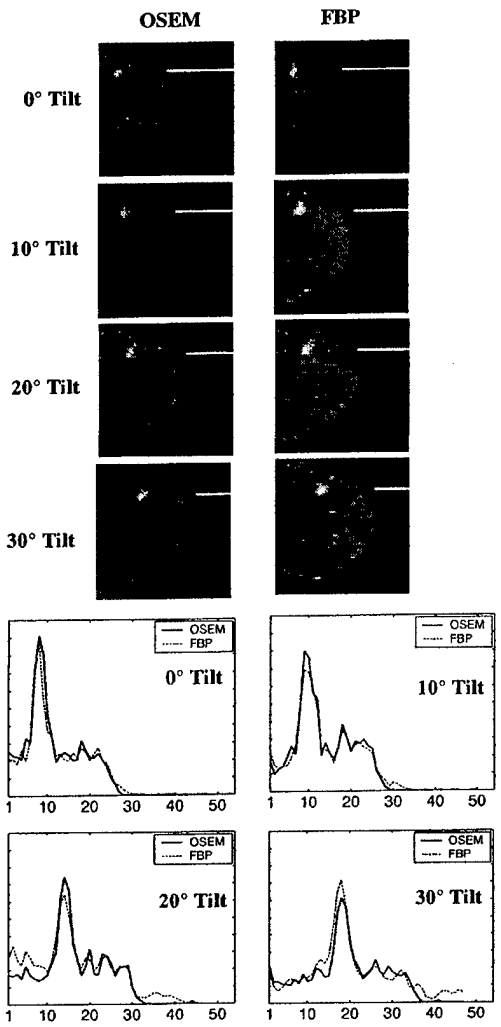

Fig. 13. Sagittal view OSEM and FBP reconstructions of anthropomorphic torso phantom combined with fillable breast phantom containing lesions. Profile markers are drawn axially across left-center of breast phantom.

TABLE I
CONTRAST AND SNR VALUES OF LARGE LESION FOR OSEM AND FBP RECONSTRUCTIONS

	SNR	Contrast	ROR (cm)
OSEM			
0°	9.98	2.65	7.47
10°	13.43	3.84	6.43
20°	12.23	2.82	5.48
30°	12.85	3.57	5.48
FBP			
0°	5.57	2.26	7.47
10°	6.39	2.13	6.43
20°	6.59	2.75	5.48
30°	9.10	3.25	5.48

best noise/bias trade-off for OSEM 0°, 15°, and 30° data and four iterations were found optimal for 45° data. OSEM reconstructions displayed the lower overall bias.

B. Defrise Disk Phantom Scan

Fig. 12 displays reconstructions of mini-Defrise phantom disks placed inside a fillable breast phantom. The resulting profiles indicate a bowing effect slightly visible at 10° tilt, and more clearly visible at 15° tilt. OSEM Defrise disk contrast was significantly better at greater tilt angles compared to FBP results. OSEM reconstruction sets displayed a one pixel (0.48 cm, 3.8%) increase in breast length at 15° tilt, measured from the nipple to the anterior wall. FBP profiles indicated a two pixel (0.98 cm, 7.6%) increase in breast length. All profiles drawn axially across the right-center of the breast indicate an increase in counts toward the nipple due to attenuating effects of the Defrise disk phantom within the breast.

C. Fillable Breast Phantom With Lesions

Table I presents contrast and SNR values for reconstructions of the fillable breast phantom containing lesions (Fig. 13). OSEM reconstructions showed greater SNR and contrast values at all tilt angles. Because camera tilt allows greater access to the breast and in turn decreases the effective ROR, overall contrast and SNR values generally increased with tilt angle, confirming

the effectiveness which can be achieved with TH-SPECT and dedicated compact gamma cameras.

IV. Discussion and Conclusion

This paper has presented a geometric derivation of the ramp filter for tilted parallel-beam geometries. FBP simulation results indicated a greater increase in artifacts with increasing tilt, as compared with iterative reconstruction, which better maintained overall breast shape. Simulation-based noise versus bias studies indicated near-optimal iteration and cut-off parameters for each method and showed less bias at a given noise for OSEM as compared to FBP. Phantom studies demonstrated consistently higher SNR and contrast values for OSEM reconstructions at all tilt angles.

TH-SPECT data do not sufficiently sample the Orlov sphere and therefore artifacts are present in all TH-SPECT reconstructions. The effect of these insufficiencies can be examined in frequency space as missing conical regions shown in Fig. 4. This "missing cone" problem has been investigated in a variety of different 3-D imaging systems with limited view angles [2], [15]–[17]. If frequency components within the missing cone and especially along the τ axis are assumed to be zero, the reconstructed mean densities of all planes perpendicular to z will be equal. This has the effect of producing unwanted activity in areas where activity should be zero or near-zero. These activity distortions are observed in FBP techniques as streak artifacts (Fig. 11) along the axis of rotation. Due to complete sampling of the $\tau = 0$ plane, transverse slices do not exhibit streak artifacts, although in-plane distortions are present.

The quality of TH-SPECT reconstructions clearly degrades with tilt angle, specifically due to the volumetric increase in null space. The fraction of null space to total frequency volume is given as

$$\frac{Null\ \ space}{Total\ \ volume} = \sin\phi. \tag{6}$$

With 30° tilt, only 13.4% of frequency space accounts for missing data. With 60° tilt, however, half of the frequency data is missing. This nonlinear increase in unsampled volume indicates tilt angles over 30° may not be useful for breast SPECT.

The conjugate views for nontilted projections exist, and, therefore, θ need only be sampled from 0 to π. For tilted projections, however, the conjugate view does not exist and θ should be sampled from 0 to 2π. This is illustrated in Fig. 3 (bottom) as rotation from 0° to 180° degrees does not even fully sample the frequency space region outside the circle of radius $\tau''\sin\phi$.

Herein, we have investigated tilted orbits in which the camera center moves along a circle, elucidating the nature of the incomplete sampling provided by these orbits and the effectiveness of FBP and OSEM in utilizing this incomplete data. In other work, we proposed circle-plus-arc [1], [4] and more elaborate orbits that do provide complete sampling of an isolated breast, and we have developed a SPECT system capable of implementing such orbits [12].

Acknowledgment

The authors would like to thank Duke Health Systems for the use of the gamma camera, N. Jaszczak and Data Spectrum Corp. for use of phantoms, and K. Greer for technical assistance with data collection.

References

[1] B. C. Pieper, J. E. Bowsher, M. P. Tornai, J. Peter, K. Greer, and R. J. Jaszczak, "Breast tumor imaging using a tiltable head SPECT camera," *IEEE Trans. Nucl. Sci.*, vol. 48, pp. 1477–1482, Aug. 2001.

[2] M. Radermacher, "Three-dimensional reconstruction of single particles from random and nonrandom tilt series," *J. Electron Microscopy Technique*, vol. 9, pp. 359–394, 1988.

[3] S. S. Orlov, "Theory of three dimensional reconstruction," *Sov. Phys. Crystallogr.*, vol. 20, no. 3, pp. 312–314, 1975.

[4] S. D. Metzler, J. E. Bowsher, M. P. Tornai, B. C. Pieper, J. Peter, and R. J. Jaszczak, "SPECT breast imaging combining horizontal and vertical axes of rotation," *IEEE Trans. Nucl. Sci.*, vol. 49, pp. 31–36, Feb. 2002.

[5] A. C. Kak and M. Slaney, *Principles of Computerized Tomographic Imaging*. New York: IEEE, 1988, ch. 9, pp. 49–112.

[6] R. N. Bracewell and A. C. Riddle, "Inversion of fan-beam scans in radio astronomy," *Astrophys. J.*, vol. 150, pp. 427–434, Nov. 1967.

[7] G. N. Ramachandran and A. V. Lakshminarayanan, "Three dimensional reconstructions from radiographs and electron micrographs: Application of convolution transforms," *Proc. Nat. Acad. Sci.*, vol. 68, pp. 2236–2240, 1971.

[8] A. Rosenfeld and A. C. Kak, *Digital Picture Processing*, 2nd ed. New York: Academic, 1982.

[9] G. T. Herman, "Emission computed tomography," in *Image Reconstruction From Projections: The Fundamentals of Computerized Tomography*, T. F. Budinger, G. T. Gullberg, and R. H. Huesman, Eds. New York: Academic Press, 1980, pp. 147–246.

[10] J. C. Russ, *The Image Processing Handbook*. Boca Raton, FL: CRC, 1999, ch. 5, pp. 305–370.

[11] J. Peter, M. P. Tornai, and R. J. Jaszczak, "Analytical versus voxelized phantom representation for Monte Carlo simulation in radiological imaging," *IEEE Trans. Med. Imag.*, vol. 19, pp. 556–564, Oct. 2000.

[12] M. P. Tornai, J. E. Bowsher, C. N. Archer, J. Peter, L. R. MacDonald, B. E. Patt, J. S. Iwanczyk, R. J. Jaszczak, and R. E. Coleman, "Dedicated breast imaging with an ASET: Application Specific Emission Tomograph," *J. Nucl. Med.*, vol. 42, no. 5, p. 97P, 2001.

[13] J. Li, R. J. Jaszczak, K. L. Greer, R. E. Coleman, Z. J. Cao, and B. M. W. Tsui, "Direct cone beam SPECT reconstruction with camera tilt," *Phys. Med. Biol.*, vol. 38, pp. 241–258, 1993.

[14] P. Grangeat, P. Masson, P. Melennec, and P. Sire, "Evaluation of the 3D Radon transform algorithm for cone beam reconstruction," *Proc. SPIE*, vol. 1445, pp. 320–331, 1991.

[15] J. Frank, *Electron Tomography*. New York: Plenum, 1992.

[16] F. Natterer, *The Mathematics of Computerized Tomography*. New York: Wiley, 1986.

[17] M. Y. Chiu, H. H. Barrett, R. G. Simpson, C. Chou, J. W. Arendt, and G. R. Gindi, "Three-dimensional radiographic imaging with a restricted view angle," *J. Opt. Soc. Amer.*, vol. 68, no. 10, pp. 1323–1333, Oct. 1979.

Effects of Lead Shielding of Background Organ Activity in Pinhole SPECT Breast Tumor Imaging

T. Lee, K. Braun, R. Jaszczak, J. Bowsher, K. Bobkov

Biomedical Engineering, Duke University, Durham, NC, U.S.A.

The objective of this study was to investigate the effect on contrast and SNR of shielding the bed with lead. Shielding reduces other-organ photon contamination, but may result in incomplete sampling of other organs and increased data inconsistency, if shielding attenuation is not modeled during reconstruction. A Trionix XLT scanner with one pinhole collimator was used to obtain experimental data on a breast phantom mounted on a torso phantom. The torso phantom contained the liver, lungs, and myocardium, all filled with varying amounts of 99mTc. The breast phantom contained two spherical lesions, also filled with 99mTc. The bed contained a cut-out for the prone breast attachment. Ten scans were performed with bed shielding, and without, in order to determine the statistical significance of the analysis. The incomplete circular orbit angular range was 186° and consisted of 94 views with a 2° step between each view. The data were then reconstructed by OSEM with 8 subsets, using up to 30 iterations without modeling shield attenuation. A 3-D region-of-interest analysis was performed on a lesion to evaluate shielding effects. The use of shielding slightly reduced noise in contrast estimates, from about 0.25 to 0.23. However, shielding increased bias in contrast from 0.24±0.08 to 0.44±0.07. SNRs were also lower with shielding. These results suggest that if shielding is to be of benefit, shielding attenuation must be modeled within iterative reconstruction.

Lead Shielding in Pinhole Breast Imaging

T. Lee, K. Braun, R. Jaszczak, J. Bowsher, K. Bobkov

Introduction:

When imaging a breast with a large field-of-view camera, a pinhole collimator is advantageous in its ability to decrease the radius-of-rotation (ROR) and get close to the breast. It has been shown that SPECT imaging of a breast phantom using a pinhole collimator has significantly reduced the effects of breast-tissue activity that overlies and underlies the lesion. [1] However, when the breast is mounted on an anthropomorphic torso phantom, increased photon contamination is introduced from the myocardium, liver and gall bladder that may impact the clarity of the breast image. The use of a pinhole collimator may obtain data with decreased photon contamination from these organs.

Although the organ of interest is the breast, the myocardium, liver, and gall bladder also take up the ^{99m}Tc-MIBI. Thus, in our phantom studies, we are investigating the difference that lead shielding will make in the contribution of photons from the outlying organs that are detected through the breast phantom by the pinhole collimator. More specifically, we are interested in determining how the radioactivity uptake in these organs affects the contrast, bias and SNR in the phantom breast images using region-of-interest (ROI) analysis.

Data Acquisition:

A Trionix XLT scanner (Trionix Research Lab, Twinsburg, Ohio) with one pinhole collimator was used to obtain the experimental data on a breast phantom mounted on an anthropomorphic torso phantom placed in a prone position on the bed. Two sets of scans were performed, each containing 10 individual scans. The first set of scans consisted of the torso phantom and all its organs filled with activity as shown in Figure 1. The second set of scans consisted of the same configuration of the torso phantom as the first scan, except with the addition of lead shielding placed over the entire table except for where the breast was located.

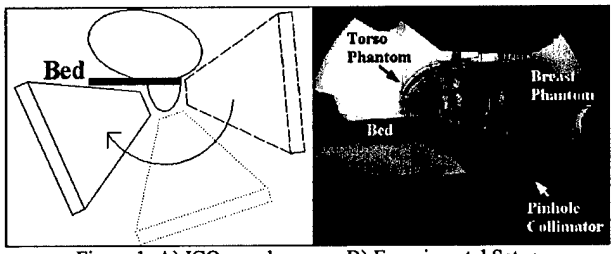

Figure 1: A) ICO angular range B) Experimental Setup

These scans had an angular range from 106^0 to 292^0. All the scans consisted of an ROR of 12.9 cm, a tungsten pinhole aperture of 3 mm, and pinhole focal length of 20 cm. All the scans consisted of 94 views with 2^0 steps between each view. The scan time per view for the first scan was 3 seconds. The scan time per view for each scan thereafter was adjusted in length for radioactive decay so that the effective scan times were the same for all the scans. A total of 20 scans were performed. Ten scans of each configuration were performed to obtain better statistical results. The projection data was stored in a grid size of 256x128 (pixel size = 1.72mm) for further processing.

Phantom Study:

The torso phantom (Model ECT/TOR/P, Data Spectrum Corp., Hillsborough, NC) contained the lungs, liver, and heart. The breast was mounted on the left side of the torso and placed in a prone position on the imaging bed. Two hollow spheres, used to simulate lesions, were placed in the breast, one approximately three centimeters below the nipple and the other close to the chest wall towards the sternum. Both had an outside diameter of 2.2 cm. This relatively large sphere size was chosen in order to assist with positioning the ROI's in the reconstructed image. The liver (volume = 1180 mL) was filled with 22.5 μCi/mL, the myocardium (volume = 118 mL) was filled with 30 μCi/mL, and the lesions (volume = 5.5 mL) were filled with 7.5 μCi/mL. The remaining parts of the torso and breast, the ventricle, and the lungs were filled with 1.5 μCi/mL. To expedite the scanning time, increased concentrations above normal clinical concentrations were used.

Data Processing:

In this initial study, the projection data were reconstructed, without shielding attenuation modeling or scattering and attenuation correction, with an OS-EM (Ordered Subset Expectation Maximization) algorithm for faster processing with minimal image quality compensation. Thirty iterations with an OS level (or the number of ordered subsets) of 8 were used over 94 projection views. The reconstructed image was in a grid size of 128x128x100 with a voxel size of 2mm.

Results and Discussion:

The reconstructed images for individual scans were relatively noisy making the ROI delineation difficult. One method to overcome this difficulty was to sum up all the individual scans for each set before reconstruction to simulate a long scan, assuming that the phantom did not move during data acquisition. The simulated long scan provided for easier ROI delineation since noise was reduced. This is shown in Figure 2. Comparison of the profiles along the white line shows that the individual scan is noisier than the long scan.

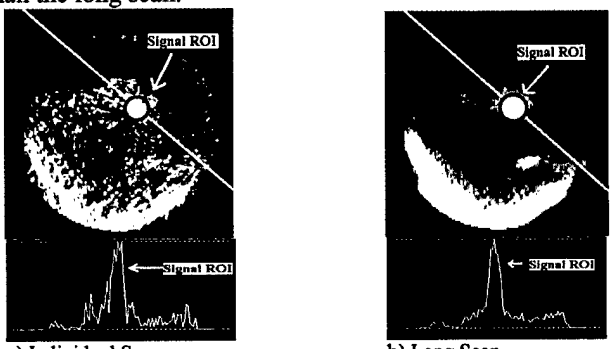

a) Individual Scan b) Long Scan

Figure 2: 1st Iteration - OSEM

ROI analysis:

The sphere closer to the chest wall was distorted in shape after reconstruction, most likely due to insufficient sampling. The circled lesion as shown in Figure 2 is used for analysis. Contrast and SNR (signal to noise ratio) values were employed to evaluate shielding effects. They can be mathematically expressed as,

$$Contrast = \frac{|N_{bg} - N_{ROI}|}{N_{bg}}, \qquad SNR = \frac{|N_{bg} - N_{ROI}|}{\sigma_{bg}}$$

where N_{ROI} and N_{BG} are the mean pixel intensity in the ROI and the background respectively, and σ_{bg} is the standard deviation in pixel intensity over the ROI.

A spherical ROI of 0.9 cm in radius was created within the lesion volume with its center at the centroid of the lesion. Statistical evaluation was highly dependent upon where the background was because scattering and attenuation were not corrected in the image. To achieve uniformity, a background mask was obtained by creating a shell of 1.2cm in thickness around the sphere ROI with a gap (0.8 cm) between the surface of the ROI mask and the inner surface of the background shell. The masks were applied to the reconstructed images from the short

scans for statistical evaluation as shown in Table 1 and Figure 3. 'Mean' value (for both contrast and SNR) is the average of 10 different scans. 'Noise' value is an estimate of the standard error of the distribution from which contrast or SNR rises. Bias is the difference between the measured contrast and the true contrast ($C_{true} = 4$).

Table 1: Shielding Effect

	Without Shielding - No Filter Applied				
	Contrast			SNR	
Iteration	Mean	Noise	Bias	Mean	Noise
1th	3.3±0.06	0.19	0.7±0.06	4.5±0.28	0.28
2nd	3.8±0.07	0.22	0.2±0.07	2.7±0.18	0.18
3rd	3.8±0.07	0.22	0.2±0.07	2.0±0.13	0.13
4th	3.8±0.07	0.22	0.2±0.07	1.6±0.11	0.11
5th	3.8±0.08	0.24	0.2±0.08	1.3±0.09	0.09
6th	3.8±0.08	0.25	0.2±0.08	1.3±0.09	0.09
7th	3.8±0.08	0.25	0.2±0.08	1.3±0.09	0.09
8th	3.8±0.08	0.26	0.2±0.08	1.3±0.09	0.09
	With Shielding - No Filter Applied				
	Contrast			SNR	
Iteration	Mean	Noise	Bias	Mean	Noise
1th	3.1±0.07	0.21	0.9±0.07	4.1±0.09	0.27
2nd	3.5±0.07	0.22	0.5±0.07	2.5±0.05	0.16
3rd	3.6±0.07	0.23	0.4±0.07	1.9±0.04	0.12
4th	3.6±0.07	0.23	0.4±0.07	1.5±0.03	0.1
5th	3.6±0.07	0.23	0.4±0.07	1.3±0.03	0.08
6th	3.6±0.07	0.23	0.4±0.07	1.2±0.03	0.08
7th	3.6±0.07	0.23	0.4±0.07	1.2±0.03	0.08
8th	3.6±0.07	0.23	0.4±0.07	1.2±0.02	0.08

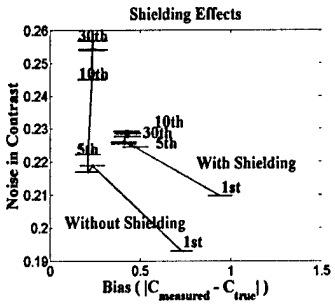

Figure 3: Noise vs. Bias

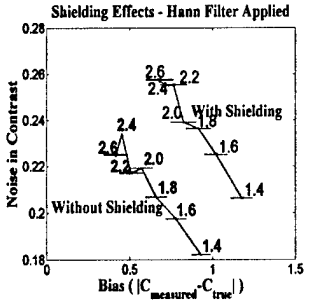

Figure 4: Filtered Noise vs. Bias

The horizontal bars represent the standard error of the mean calculated by dividing the noise by $\sqrt{N}$, where $N = 10$ is the number of individual scans.

It is expected that with an OS-EM algorithm, the higher the iteration number, the noisier and the closer to the true contrast the image is. Such characteristics are shown in both shielded and non-shielded cases, although the effect is very subtle. To observe such behavior more clearly, 3-D filtering was applied to the 20th iteration of the reconstructions. The Hann filter as described below was used with different cutoff (vc) values and the results are tabulated in Table 2, and the Noise vs. Bias plot is shown in Figure 4. Since filtering makes the bias higher, we expected the plot to resemble an inversely proportional curve. The results are mostly consistent with our predictions.

$$H(v) = 0.5*(1+\frac{\cos(\pi v)}{vc})$$

From both Figure 3 and Figure 4, it is clear that shielded images are more biased. A comparison between shielded and non-shielded projection views, shown in Figure 5, reveals that the non-shielded scans contain a higher number of counts from approximately 180 to 260 degrees. From the plot it is clear that the lead plate is moderately effective in reducing counts from background scattering.

Table 2: Shielding and Filtering

	Without Shielding - Hann Filter Applied				
Cutoff(vc)	Contrast			SNR	
cycles/cm	Mean	Noise	Bias	Mean	Noise
1.4	3.1±0.06	0.18	0.9	10±0.3	0.81
1.6	3.2±0.06	0.2	0.8	9.2±0.2	0.72
1.8	3.3±0.07	0.21	0.7	8.2±0.2	0.63
2	3.4±0.07	0.22	0.6	7.3±0.2	0.52
2.2	3.5±0.07	0.22	0.5	6.5±0.1	0.44
2.4	3.5±0.07	0.23	0.5	5.8±0.1	0.4
2.6	3.6±0.07	0.22	0.4	5.3±0.1	0.36
	With Shielding - Hann Filter Applied				
Cutoff(vc)	Contrast			SNR	
cycles/cm	Mean	Noise	Bias	Mean	Noise
1.4	2.8±0.07	0.21	1.2	9.2±0.3	1
1.6	3±0.07	0.22	1	8.4±0.3	0.85
1.8	3.1±0.07	0.24	0.9	7.5±0.2	0.71
2	3.2±0.08	0.24	0.8	6.7±0.2	0.61
2.2	3.2±0.08	0.26	0.8	6.0±0.2	0.51
2.4	3.3±0.08	0.26	0.7	5.4±0.1	0.43
2.6	3.3±0.08	0.26	0.7	4.8±0.1	0.37

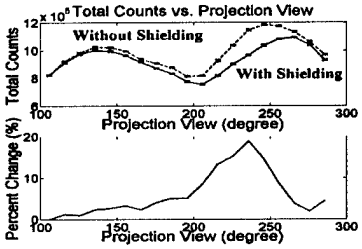

Figure 5: Counts in Projection Views

However, our findings in Figure 3 and Figure 4 are in contradiction with those in Figure 5. Reduction in background counts (Figure 5) is expected to decrease bias and increase SNR, but the bias and SNR evaluations prove otherwise. The use of shielding slightly reduced SNR from about 1.3 ± 0.09 to 1.2 ± 0.02 on the 7th iteration. However, shielding increased bias in contrast from 0.2 ± 0.08 to 0.4 ± 0.07. We believe that this obvious discrepancy may be due to inconsistency in projection data, or to incomplete sampling of the other organs. As the gamma camera on Triad system rotates around the phantom, significant difference in counts rises when the camera level changes from 'below the lead shielding' to 'above the lead shielding'. With our current reconstruction algorithm, this inconsistency in projection data might have introduced artifacts that lead to undesirable reconstruction results.

Conclusion:

In this study, we investigated the effects of lead shielding on breast imaging. Our results indicate that shielding is moderately effective in reducing the background counts suggesting potentials to improve lesion detectibility. However, the standard reconstruction algorithms such as OS-EM and ML-EM are limited in reconstructing inconsistent projection data. Comparison of contrast and SNR between shielded and non-shielded images revealed that contrast and SNR is significantly lower with lead shielding than without lead shielding. Future research is required to determine whether an OS-EM algorithm can be implemented that can effectively account for inconsistent projection data.

Acknowledgement

This research was supported by the National Cancer Institute of the National Institutes of Health under Grant R01-CA076006, and by the U.S. Army Medical Research Acquisition Activity of Department of Defense under Grant DAMD17-01-1-0226.

References

1. Scarfone C, Jaszczak RJ, Li J, Soo MS, Smith MF, Greer KL, Coleman RE. Breaat tumour imaging using incomplete circular orbit pinhole SPET: A phantom study. Nuc Med Comm 1997; 18:1077-1086.